Mechanistic insights into NO-H_2 reaction over Pt/boron-doped graphene catalyst

Zhenhua Yao, Lei Li, Xuguang Liu, Kwun Nam Hui, Ling Shi, Furong Zhou, Maocong Hu, K.S. Hui

PII: S0304-3894(20)32317-7

DOI: https://doi.org/10.1016/j.jhazmat.2020.124327

Reference: HAZMAT124327

To appear in: *Journal of Hazardous Materials*

Received date: 24 July 2020
Revised date: 16 October 2020
Accepted date: 17 October 2020

Please cite this article as: Zhenhua Yao, Lei Li, Xuguang Liu, Kwun Nam Hui, Ling Shi, Furong Zhou, Maocong Hu and K.S. Hui, Mechanistic insights into NO-H_2 reaction over Pt/boron-doped graphene catalyst, *Journal of Hazardous Materials,* (2020) doi:https://doi.org/10.1016/j.jhazmat.2020.124327

Mechanistic insights into NO-H_2 reaction over Pt/boron-doped graphene catalyst

Zhenhua Yao[a], Lei Li[b], Xuguang Liu[c], Kwun Nam Hui[d], Ling Shi[a], Furong Zhou[a], Maocong Hu[a,*], K.S. Hui[e,*]

[a] Hubei Key Laboratory of Industrial Fume and Dust Pollution Control, and Key Laboratory of Optoelectronic Chemical Materials and Devices of Ministry of Education, Jianghan University, Wuhan 430056, China

[b] Key Laboratory of Extraordinary Bond Engineering and Advanced Materials Technology (EBEAM) of Chongqing, Yangtze Normal University, Chongqing 408100, China

[c] College of Materials Science and Engineering, Qingdao University of Science and Technology, Qingdao 266042, China

[d] Institute of Applied Physics and Materials Engineering (IAPME) University of Macau Avenida da Universidade, Taipa, Macau, China

[e] School of Engineering, University of East Anglia, Norwich, NR4 7TJ, United Kingdom

[*]Corresponding author

E-mail: maocong.hu@jhun.edu.cn (M. Hu), k.hui@uea.ac.uk (K.S. Hui)

Tel: +86 189 7112 8395

Abstract

This work presents a systematical experimental and Density Functional Theory (DFT) studies to reveal the mechanism of NO reduction by H_2 reaction over platinum nanoparticles (NPs) deposited on boron-doped graphene (denoted as Pt/BG) catalyst. Both characterizations and DFT calculations identified boron (in Pt/BG) as an additional NO adsorption site other than the widely recognized Pt NPs. Moreover, BG led to a decrease of Pt NPs size in Pt/BG, which facilitated hydrogen spillover. The mathematical and physical criteria of the Langmuir-Hinshelwood dual-site kinetic model over the Pt/BG were satisfied, indicating that adsorbed NO on boron (in Pt/BG) was further activated by H-spillover. On the other hand, Pt/graphene (Pt/Gr) demonstrated a typical Langmuir-Hinshelwood single-site mechanism where Pt NPs solely served as active sites for NO adsorption. This work helps understand NO-H_2 reaction over Pt/BG and Pt/Gr catalysts in a closely mechanistic view and provides new insights into roles of active sites for improving the design of catalysts for NO abatement.

Keywords: NO abatement, kinetic modelling, DFT study, Langmuir-Hinshelwood dual-site mechanism, graphene-based catalysis

Nomenclature

BG	boron-doped graphene	Pt/BG	platinum supported BG
Pt/Gr	platinum supported graphene	Pt_4	Pt cluster model in Pt/BG for DFT
Pt_{13}	Pt cluster model in Pt/Gr for DFT	$C_{NO,0}$	concentrations of NO at the feed
C_{NO}	concentrations of NO at outlet	r_{NO}	reaction rates of NO
X_{NO}	conversion of nitric oxide	W	catalyst weight
v	total gas flow rate	E_a	activation energy
A	pre-exponential factor	ΔS	adsorption entropy
ΔS^0_g	standard gas phase entropy	ΔH	adsorption enthalpy
R	universal gas constant	T	temperature in Kelvin (K)
k_i	reaction rate constant	K_i	adsorption equilibrium constant
*	Pt site	#	doped-boron site

1. Introduction

Nitric oxide (NO) is a major pollutant produced in the combustion of fossil fuels. It is not only harmful to human health but causes persistent changes in the biosphere [1, 2]. Selective catalytic reduction (SCR) of nitric oxide with reductants like H_2, CO, NH_3, or hydrocarbons was widely investigated to limit its release [3-12]. H_2-SCR is considered as a promising approach for NO removal due to its high activity at low temperatures (T<200 °C), which is attractive for applications such as cold start conditions or lean-burn diesel engines, where the exhaust temperature has become lower and lower for improving engine thermal efficiency [13-15]. Moreover, the low H_2 concentration (< 1%) and operation temperature suggest H_2-SCR is a safe

technology. Numerous supported/doped/encapsulated noble metal catalysts were already proposed and tested for H_2-SCR [16-23], while different reaction mechanisms were presented.

H_2 dissociative adsorption was generally considered to be occurring on metal sites, while H-spillover from the metal surface to vicinity of support was usually invoked to describe the reaction mechanism [24-26]. However, the involvement of H-spillover in developing the kinetic model for NO-H_2 reaction was rarely reported except the very recent work [27], where Eley-Rideal mechanism was used to describe the reaction route, i.e. gas NO reacts with adsorbed H-spillover. More commonly, Langmuir-Hinshelwood mechanism is employed for the model development due to widely accepted agreement about the presence of NO* at kinetically-consequential coverages, where the metal site (*) was considered to be responsible for NO and H_2 co-adsorption and surface reactions [28-37]. Consequently, almost all the derived kinetic equations were actually based on the Langmuir-Hinshelwood single-site mechanism. Another debated issue with NO-H_2 reaction mechanism is that the N-O bonds activation pathways remain controversial. In fact, experimental and density functional theory (DFT) studies indicated different elementary steps for NO activation [38-47]. Generally, six types of activation modes were proposed (* represents active site, v is vacancy) [32, 34, 35]: (i) direct NO* dissociation (Eq. (1)); (ii) adjacent adsorbed NO* attack (Eq. (2)); (iii) H-assisted NO* activation (Eq. (3)); (iv) N-O cleavage with sequential addition of two chemisorbed H-atoms (Eq. (4)-(5)); (v) H_2* involved NO* activation (Eq. (6)); and (vi) O vacancy induced NO* activation (Eq. (7)). Consequently, the detailed reaction mechanism for NO reduction by H_2 still remains unsettled.

$$\mathrm{NO}* + * \rightarrow \mathrm{N}* + \mathrm{O}* \quad (1)$$

$$\mathrm{NO}* + \mathrm{NO}* \rightarrow N_2\mathrm{O}* + \mathrm{O}* \quad (2)$$

$$\mathrm{NO}* + \mathrm{H}* \rightarrow \mathrm{N}* + \mathrm{OH}* \quad (3)$$

$$NO* + H* \leftrightarrow HNO* + * \quad (4)$$

$$HNO* + H* \rightarrow *HNOH* \quad (5)$$

$$NO* + H_2* \rightarrow NH* + OH* \quad (6)$$

$$NO* + v \rightarrow N* + O \quad (7)$$

In the previous work, we demonstrated a strategy to design and prepare platinum supported boron-doped graphene (Pt/BG) catalysts for H_2-SCR [48]. On the basis of the systematic characterizations of catalyst structure, measurement of chemisorption ability to NO and H_2, and superior performance for H_2-SCR reaction, we proposed a bifunctional catalytic mechanism of H_2-SCR over the Pt/BG catalyst. Both metallic Pt and doped boron served as the active sites for NO adsorption, while Pt sites solely contributed to H_2 adsorption with spillover. Obviously, the reaction mechanism was described qualitatively there.

Herein, we combined experimental and DFT studies as well as kinetic modelling of NO reduction by H_2 on the Pt/BG catalyst to mediate the reaction as well as fully understand the role of boron in the Pt/BG on the reaction mechanism. For this purpose, both Pt/BG and platinum supported graphene (Pt/Gr) catalysts were synthesized and characterized. Steady-state kinetic rate data were collected at four temperature points. Integrating H-spillover in kinetical coverages, Langmuir-Hinshelwood dual-site kinetic model (denoted as L-H_d) based on H-assisted dissociative adsorption of NO over both Pt and doped boron sites as the rate-determining step was successfully developed over the Pt/BG case. It was further validated by both mathematical and physical criteria. In contrast, Langmuir-Hinshelwood single-site kinetic model (denoted as L-H_s) was established that considers Pt site only contributing to the kinetics of NO-H_2 reaction in the Pt/Gr case. Furthermore, DFT calculations confirmed the experimental observations and

kinetic parameters for both cases. This work provides new insights into a deeper understanding of NO-H_2 catalytic reaction over the Pt/BG and Pt/Gr in a closely mechanistic view.

2. Experimental

2.1. Catalysts Preparation and Characterization

The detailed preparation procedures were reported in the previous work [48]. Briefly, a one-pot hydrothermal method was employed with homemade graphene oxide (GO, Figure S1) as the substrate while $Pt(NH_3)_4(NO_3)_2$ and boric acid were used as Pt and boron sources, respectively. The added amount of $Pt(NH_3)_4(NO_3)_2$ and boric acid was determined by the weight ratio of boron/(boron+carbon)=20% and Pt/(Pt+carbon)=1%, respectively. Pt/Gr and boron-doped graphene (BG) was prepared in the same hydrothermal condition without adding boric acid or $Pt(NH_3)_4(NO_3)_2$, respectively. ICP, XPS, CO-chemisorption, H_2-TPD, and NO-TPD were carried out to investigate the structure of the graphene matrix, dispersion and size of Pt NPs, and chemisorption ability to nitric oxide and hydrogen, respectively. Characterizations details can be found in Supporting Information.

2.2. Steady-State Kinetic Study

Selective catalytic reduction of NO by H_2 at atmospheric pressure was conducted in a tubular fixed-bed reactor, where steady-state data are collected for the evaluation of the kinetic parameters [49, 50]. NO and H_2 with specific concentration balanced by helium were introduced by mass flow controllers (MFC, calibrated using a soap bubble flow meter) into a mixer before flowing into the top of the reactor. The temperature of the catalyst bed was monitored by a temperature controller with a thermocouple inserted in the bed. Granular Pt/BG or Pt/Gr catalyst

(~65 mg) diluted with γ-alumina was stabilized on quartz wool which was supported by SiC. To eliminate the internal mass-transfer effect, the catalyst size of 100–150 mesh was selected to provide the catalyst bed height to a catalyst particle size ratio of $L/D_p \geq 50$ as well as reactor internal diameter to a catalyst particle size ratio of $D/D_p \geq 30$ [49, 51]. External mass transfer limitation was excluded by increasing the inlet flow rate until the reaction rate remained almost unchanged [49]. The eliminations of external and internal diffusion limitations were further confirmed by Mears (C_M) and Weisz–Prater (C_{WP}) criteria, respectively [52-54] (the detailed calculations are presented in the Supporting Information). The total flow rate was set at 200 mL/min (i.e., 3.33×10^{-6} m^3 s^{-1}) with a GHSV of about 80,000 h^{-1} for all runs with different NO concentrations (602–1605 ppm, i.e., 0.0248–0.0661 mol m^{-3}) and fixed H_2 concentration (1600 ppm, i.e., 0.0659 mol m^{-3}). The reaction tests were performed at four temperature points (300, 310, 320, and 330 K) under atmospheric pressure (Table 1).

Table 1 Experimental conditions and results of the steady-state kinetic study [a]

Temperature (K)	Pt/Gr				Pt/BG			
	$C_{i,0}$ (mol m^{-3}) [b]		C_i (mol m^{-3}) [c]		$C_{i,0}$ (mol m^{-3}) [b]		C_i (mol m^{-3}) [c]	
	NO	H_2	NO	H_2	NO	H_2	NO	H_2
300	0.0248	0.0659	0.0204	0.0615	0.0248	0.0659	0.0202	0.0613
300	0.0330	0.0659	0.0289	0.0618	0.0330	0.0659	0.0285	0.0615
300	0.0413	0.0659	0.0373	0.0619	0.0413	0.0659	0.0369	0.0615
300	0.0496	0.0659	0.0459	0.0622	0.0496	0.0659	0.0453	0.0617
300	0.0578	0.0659	0.0543	0.0625	0.0578	0.0659	0.0538	0.0619
300	0.0661	0.0659	0.0639	0.0637	0.0661	0.0659	0.0633	0.0631

310	0.0248	0.0659	0.0201	0.0613	0.0248	0.0659	0.0197	0.0611
310	0.0330	0.0659	0.0285	0.0614	0.0330	0.0659	0.0282	0.0612
310	0.0413	0.0659	0.0369	0.0615	0.0413	0.0659	0.0366	0.0613
310	0.0496	0.0659	0.0453	0.0617	0.0496	0.0659	0.0450	0.0615
310	0.0578	0.0659	0.0537	0.0619	0.0578	0.0659	0.0534	0.0617
310	0.0661	0.0659	0.0632	0.0630	0.0661	0.0659	0.0630	0.0629
320	0.0248	0.0659	0.0198	0.0610	0.0248	0.0659	0.0195	0.0608
320	0.0330	0.0659	0.0282	0.0612	0.0330	0.0659	0.0279	0.0610
320	0.0413	0.0659	0.0365	0.0613	0.0413	0.0659	0.0363	0.0611
320	0.0496	0.0659	0.0450	0.0615	0.0496	0.0659	0.0448	0.0613
320	0.0578	0.0659	0.0534	0.0616	0.0578	0.0659	0.0532	0.0615
320	0.0661	0.0659	0.0630	0.0629	0.0661	0.0659	0.0628	0.0628
330	0.0248	0.0659	0.0194	0.0605	0.0248	0.0659	0.0191	0.0606
330	0.0330	0.0659	0.0278	0.0607	0.0330	0.0659	0.0276	0.0608
330	0.0413	0.0659	0.0362	0.0608	0.0413	0.0659	0.0359	0.0608
330	0.0496	0.0659	0.0447	0.0610	0.0496	0.0659	0.0445	0.0611
330	0.0578	0.0659	0.0531	0.0612	0.0578	0.0659	0.0529	0.0612
330	0.0661	0.0659	0.0627	0.0625	0.0661	0.0659	0.0626	0.0626

[a] Kinetic data were collected over two catalysts, Pt/Gr and Pt/BG, independently;

[b] Feed concentrations of nitric oxide and hydrogen, $C_{i,0}$, i is NO or H_2, which refers to NO or H_2;

[c] Outlet concentrations of nitric oxide and hydrogen, C_i, i is NO or H_2, which refers to NO or H_2;

Reactants in the inlet and products in the effluent were analyzed with an on-line mass spectrometer (Agilent 7010A) [55, 56]. The MS signal of each gas was converted to corresponding concentrations by a pre-determined calibration line. All data were collected under steady-state, while the average value of three sets of independent experiments (deviations within ±5%) was reported in Table 1. The conversion of NO (X_{NO}) was calculated using Eq. (8), where $C_{NO,0}$ and C_{NO} represent the concentrations of NO at the inlet and effluent, respectively. Kinetic experiments were performed in an operational regime of low conversion (typically less than 20 %) and far from equilibrium conditions [57]. Only N_2 and N_2O were detected as the N-containing product species. Nitrogen balance was calculated for each run using Eq. (9), where $[NO]_{in}$ is the NO molar flow rate in feed, $[NO]_{out}$, $[N_2O]$, and $[N_2]$ are the NO, N_2O, and N_2 molar flow rates in the effluent stream, respectively. The N-balance was observed to be close to 100% for all experiments. The steady-state reaction rate was calculated using Eq. (10), where r_{NO}, $C_{NO,0}$, v, X_{NO}, and W are the steady-state NO reaction rate, NO feed concentration, total gas flow rate, steady-state NO conversion, and catalyst weight, respectively.

$$X_{NO} = \frac{C_{NO,0} - C_{NO}}{C_{NO,0}} \times 100\% \quad (8)$$

$$[NO]_{in} = [NO]_{out} + 2[N_2O] + 2[N_2] \quad (9)$$

$$r_{NO} = \frac{C_{NO,0} v X_{NO}}{W} \quad (10)$$

2.3. Kinetics Data Analysis

Similar data fitting method and model discrimination criteria were used as reported in our previous work [58]. Briefly, a power-law model was first established for both Pt/BG and Pt/Gr cases. Langmuir-Hinshelwood dual-site (denoted as L-H_d) and single-site kinetic model (denoted

as L-H_s) were developed for Pt/BG and Pt/Gr cases, respectively. Kinetic parameters estimation (reaction rate constant *k*, reaction order, and adsorption equilibrium constant *K*) was performed by fitting each model to the experimental data. Curve-fitting applications with the Levenberg–Marquardt method of MATLAB R2014a and Microsoft Excel Solver were employed for the calculations. Nonlinear least squares regression was used to minimize the sum of squared errors between the experimental rates $r_{exp.,n}$ and the values predicted by the kinetic models $r_{cal.,n}$ as much as possible (Eq. (11)). Moreover, the correlation coefficient (r^2) was used to intuitively distinguish each model [59, 60].

$$\min \sum_{1}^{n} \left(r_{exp.,n} - r_{cal.,n}\right)^2 \tag{11}$$

Pre-exponential factor *A* and activation energy E_a as well as NO and H_2 adsorption enthalpy ΔH_{NO} and ΔH_{H_2}, and NO and H_2 adsorption entropy ΔS_{NO} and ΔS_{H_2}, if applicable, were determined by Arrhenius and Van't Hoff equations using linear regression with Eqs. (12) and (13). R is the universal gas constant 8.314 J K^{-1} mol^{-1}, and T is the reaction temperature in Kelvin (K).

$$lnk = lnA + \left(\frac{-E_a}{R}\right)\frac{1}{T} \tag{12}$$

$$lnK = \left(\frac{-\Delta H}{R}\right)\frac{1}{T} + \frac{\Delta S}{R} \tag{13}$$

The physical meaning of the derived ΔH and ΔS were further examined with the criteria as listed in Eqs. (14) and (15) for catalytic reactions [61-64]. Eq. (14) indicates that the loss of entropy -ΔS^0_{ads} during catalytic adsorption should be higher than 41.9 J mol^{-1} K^{-1} but lower than the standard gas-phase entropy ΔS^0_g (210 and 141 J mol^{-1} K^{-1} for NO and H_2, respectively) [35]. Moreover, loss of entropy -ΔS^0_{ads} and adsorption enthalpy ΔH^0_{ads} follow the constraint as

demonstrated in Eq. (15) for molecules strongly bounding on the surface, i.e. chemisorption. Violation of either above physical criteria suggested that the derived values from the proposed kinetic model are physically meaningless, indicating that an improper kinetic model may be selected.

$$41.9 < -\Delta S_{ads}^{0} < \Delta S_{g}^{0} \quad (14)$$

$$-\Delta S_{ads}^{0} < 51.1 - 1.4\Delta H_{ads}^{0} \quad (15)$$

2.4. Computational Methods

DFT calculations were performed using the Vienna Ab-initio Simulation Package (VASP) code [65-68]. For the total energy calculations, the plane wave cutoff energy was 400 eV. Ion–electron interactions were represented by ultrasoft pseudopotentials within the framework of the projector-augmented wave (PAW) method [69]. The generalized gradient approximation (GGA) with the Perdew–Burke–Ernzerhof (PBE) functional was adopted as the exchange-correlation functional [69, 70]. The Brillouin zone integration was approximated by a sum over specially selected k-points using the 3×3×1 MonkhorstPack method [71]. The geometries were optimized until the energy was converged to 5×10^{-6} eV/atom and the forces to 0.02 eV/Å. Graphene and boron-doped graphene are modeled by *p*(5×5) or *p*(6×6) supercell. In order to eliminate the interactions between slabs, the vacuum region is set to 15 Å in the z direction to separate the slabs. The adsorption energies at a temperature of 0 K and a reaction temperature of 320 K were calculated, respectively; the detailed calculation procedures were provided in the Supporting Information.

3. Results and Discussion

3.1. Experimental Observations

The multi-roles of boron were first investigated by the catalyst characterizations. The detailed data including ICP, XPS, CO-chemisorption, H_2-TPD, and NO-TPD are illustrated in Figure S2-4 and Table S1 in Supporting Information. Composition analysis from ICP and XPS confirmed that the presence of boron in Pt/BG while the XPS spectra indicated the successful embedment of boron in the graphene matrix. CO-chemisorption suggested that the size of Pt clusters on the Pt/BG (2.3 nm) is much smaller than that of the Pt/Gr (4.5 nm). Heteroatom (like boron in this work) doping usually produces a large number of defect sites, serving as anchoring sites for Pt clusters [72-74]. It generally increases the interaction between Pt clusters and boron-doped graphene, which in turn promotes Pt dispersion as well as leads to the smaller size of Pt clusters. H_2-TPD further showed that the Pt/BG had an increased number of exposed Pt, which is in good agreement to the findings of CO-chemisorption measurements. Moreover, hydrogen spillover was obviously observed on the Pt/BG while it's unnoticeable in the Pt/Gr case. The amount of H-spillover accounts for 18.87% of the total adsorbed H determined with curve deconvolution as shown in Figure S3. As concluded by Stuckert et al. [75], dispersion into ~2 nm clusters is necessary to facilitate H-spillover on Pt/carbon. The size of Pt clusters in the Pt/BG is within the range while that over the Pt/Gr is too large. NO-TPD (Figure S4) illustrated the strong affinity between NO and BG, while its desorption temperature is close to that of Pt/Gr, indicating that boron is an active site for NO chemisorption. Moreover, the amount of adsorbed NO over the Pt/BG is more than that of Pt/Gr, which may be the co-contributions from both higher Pt dispersion and additional boron sites.

3.2. Theoretical Calculations

DFT calculations were carried out to collect more information about the catalytic systems. We first calculated the adsorption energies of NO and H_2 over graphene surface (Figure S5) as listed in Table S2. Both gases showed a very weak affinity with graphene (with adsorption energies of 64.0 and 46.9 kJ mol $^{-1}$, respectively), which is consistent with the observations by H_2-TPD and NO-TPD. Thus, the adsorption of NO/H_2 over the Pt/Gr would be attributed to the Pt clusters only. In DFT calculations, two classical configurations with the different number of Pt atoms were proposed by different groups for the Pt clusters on graphene-based supports: Pt_{13} and Pt_4 [76-83]. As revealed by the above CO-chemisorption, Pt clusters of Pt/Gr and Pt/BG have different sizes (4.5 vs. 2.3 nm). Therefore, Pt_{13} and Pt_4 models were adopted for the Pt/Gr and Pt/BG, respectively, in the current DFT study. The optimized structures of Pt/Gr and NO/H_2 co-adsorption on the Pt/Gr were illustrated in Figure 1(a) and (b), respectively. The binding energy of Pt_{13} clusters with pristine graphene and adsorption energy of NO and H over the Pt/Gr were listed in Table 2. The binding energy was determined to be -211.7 kJ mol^{-1}, which is close to the value (-2.08 eV, i.e. -200.35 kJ mol^{-1}) in the literature [78, 79]. The adsorption energy of NO is -198.1 kJ mol^{-1}, which is higher than that calculated with 0.25 monolayer (ML) coverage of NO over Pt (111) surface (-1.88 eV, i.e. -181.08 kJ mol^{-1}) [38]. But it's still reasonable that the adsorption energy increases with the decrease of coverage when 1/13 ML was used in the current work. As shown in Figure 1(b), H_2 dissociatively adsorbs on the Pt/Gr while two H atoms are the active species on Pt_{13} clusters (with coverage of 2/13). The adsorption energy was determined to be -60.7 kJ mol^{-1}, which is lower than the value with ML of 0.25 in the literature (~-120 kJ mol^{-1}) but it is still reasonable [84]. The consistent DFT calculations results over the Pt/Gr with

literature further confirmed that both NO/H_2 were adsorbed on Pt sites, which led to a L-H_s mechanism-based reaction kinetics.

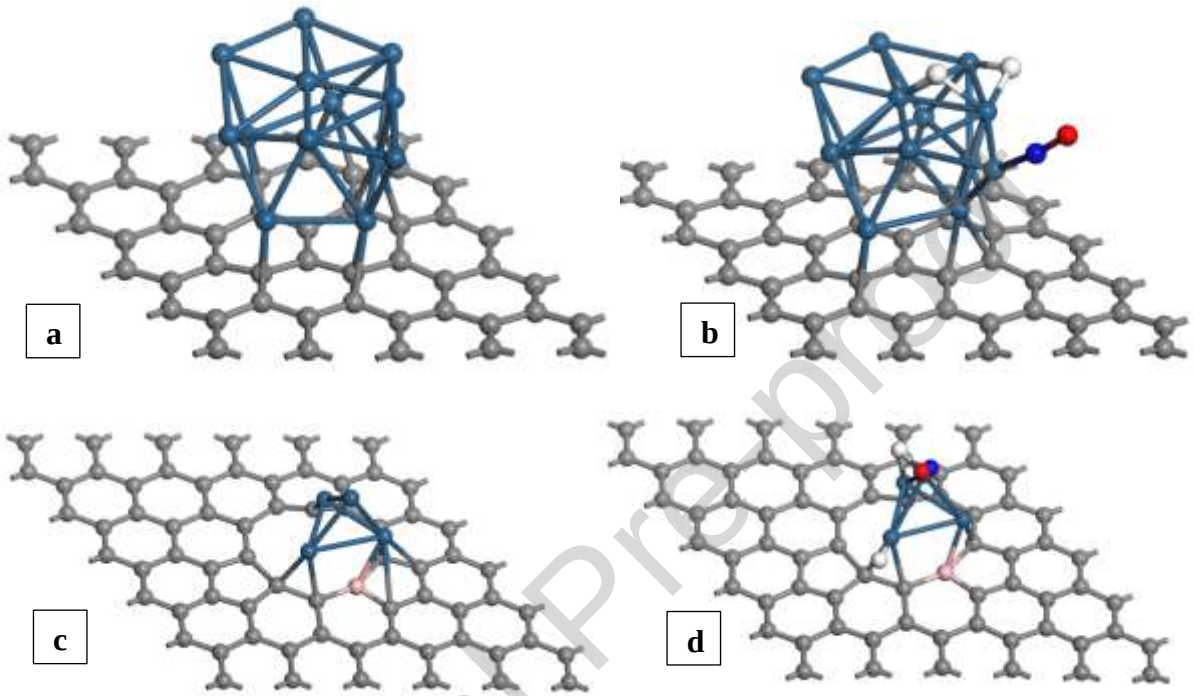

Figure 1. Optimized structures of Pt/Gr model (a), NO/H_2 co-adsorption on Pt/Gr (b), Pt/BG model (c), NO/H_2 co-adsorption on Pt/BG (d). (Gray, C; Blue, Pt; Sapphire, N; Red, O; White, H; Pink, B)

The configuration of the Pt/BG is a little bit complicated compared to the Pt/Gr case as different doping models were proposed for boron-doped graphene [85-88]. In this work, five models from literature or homemade were tested as illustrated in Figure S6-11: (i) 0/B-Gr: doped graphene with one boron atom embedment in the $p(5\times5)$ supercell without any defect site; (ii) 0/2B-Gr: doped graphene with two boron atoms embedment in the $p(5\times5)$ supercell without any defect site; (iii) 1/B-Gr: doped graphene with one boron atom embedment in the $p(6\times6)$

supercell with one defect site; (iv) 2/B-Gr: doped graphene with one boron atom embedment in the *p*(6×6) supercell with two defect sites; (v) 3/B-Gr: doped graphene with one boron atom embedment in the *p*(6×6) supercell with three defect sites. (vi) 4/B-Gr: doped graphene with one boron atom embedment in the *p*(6×6) supercell with four defect sites. The *p*(6×6) supercell instead of *p*(5×5) one was selected for the models with defects in consideration of the structure stabilization. After the optimization of each model, the adsorption configuration of NO over the models was established. The adsorption energy was further calculated as listed in Table S2. It was employed to validate the configuration by comparing it with the experimental observations (NO-TPD indicating the chemisorption of NO over the BG) as well as using calculated values from the Pt/Gr as reference. The adsorption of NO over the 0/B-Gr cannot be ascribed to chemisorption due to the positive adsorption energy (18.0 kJ mol^{-1}), which is ruled out for further consideration. The 0/2B-Gr showed a slightly strong bound strength to NO compared to the 0/B-Gr (-34.4 kJ mol^{-1}), while it's still weak for a catalytic reaction. Heteroatom-doped graphene usually contains different number of defects. Herein, four models with different number (1, 2, 3, and 4) of carbon-vacancy defect were proposed. All three models demonstrated the ability to chemisorb NO via the formation of B-N bond with adsorption energies of -10.6, -161.0, -230.9, and -698.0 kJ mol^{-1} for the 1/B-Gr, 2/B-Gr, 3/B-Gr, and 4/B-Gr respectively. Very close desorption temperature was observed for the BG and Pt/Gr in NO-TPD, indicating that both may have comparable adsorption energy. Therefore, the 3/B-Gr model was selected for the BG, which has the closest adsorption energy with the Pt/Gr (-198.1 kJ mol^{-1}).

We further optimized the structure of the Pt/BG (Pt_4 adopted for Pt cluster as discussed above) and the configuration of NO/H_2 co-adsorption as demonstrated in Figure 1(c) and (d), respectively. The binding energy of Pt_4 clusters over the BG and adsorption energies of NO and

H_2 over the Pt/BG were listed in Table 2. The high binding energy (-586.0 kJ mol^{-1}) indicated the strong interaction between Pt_4 clusters and boron-doped graphene, which accounts for the high dispersion of Pt NPs over the Pt/BG as observed by CO-chemisorption. The adsorption energies of NO and H over the Pt/BG were determined to be -191.1 and -48.6 kJ mol^{-1}, respectively. Both are lower than those from the Pt/Gr case. A stronger binding of Pt cluster to the substrate obviously leads to a greater downshift of the cluster d-band center and further decreases the adsorption energies of NO and H_2, which has been reported in the case of CO over Pt clusters [77]. Although the binding strength of Pt_4 cluster to H decreases, dissociative adsorption of H_2 is still observed on the Pt/BG as shown in Figure 1(d). Moreover, the medium bonding may benefit H-spillover, which was evidenced by the H_2-TPD (Figure S3). Previous work by Wu et al. also suggested that boron-doped graphene sheet facilitated both H migration and diffusion processes, resulting in enhanced H-spillover [89]. We also tested the Pt_4-0/B-Gr model to further validate the introduction of defects for the BG although neither NO nor H_2 was chemisorbed on the 0/B-Gr. The model and the configurations of NO/H_2 co-adsorption on the model were illustrated in Figure S12, while the binding energy of Pt_4 cluster and adsorption energy of NO/H were listed in Table S2. The binding energy (-251.3 kJ mol^{-1}) of Pt_4-0/B-Gr is in good agreement to the reported value (-2.379 eV, i.e. -229.15 kJ mol^{-1}) [89]. However, it appears to be close to the binding energy in the Pt/Gr case (-211.7 kJ mol^{-1}), suggesting that both may have similar Pt dispersion while it's not true based on the above experimental investigations. As a result, Pt_4-0/B-Gr was ruled out for the consideration as the model for the Pt/BG.

Table 2 Adsorption energies of NO and H_2, and binding energy of Pt clusters over different sample by DFT calculations, kJ mol^{-1}

Species	Sample	
	Pt/Gr [a]	Pt/BG [b]
NO	-198.1	-191.1
H [c]	-60.7	-48.6
Pt	-211.7	-586.0

[a] Pt_{13} was selected as the model for Pt clusters in the Pt/Gr case

[b] Pt_4 was selected as the model for Pt clusters in the Pt/BG case

[c] H is the active species after H_2 dissociative adsorption

Based on the above systematic investigations, Pt_4-3/B-Gr, Pt_4 clusters supported doped graphene with one boron atom embedment in the $p(6\times6)$ supercell with three defect sites, was selected as the model for the Pt/BG. Moreover, DFT calculations indicated that H_2 dissociatively adsorbed on Pt_4 sites to produce active H which further migrated and diffused to the graphene sheet by H-spillover. NO chemisorbed on both Pt_4 and boron site, which may be activated by the adjacent adsorbed-H and H-spillover, respectively. Therefore, a L-H_d mechanism was adopted for the kinetic model development.

3.3. Kinetic Study

Relatively low temperatures (300, 310, 320, and 330 K) and high gas flow rate were selected for kinetic data collection since high conversion would be achieved at high-temperature for NO reduction by H_2 [48]. As a result, the typical NO conversion was less than 20%. Power law-

based models were first developed to acquire more information about the catalytic systems over the Pt/Gr and Pt/BG. Then, detailed L-H_s and L-H_d mechanism-based models were established for the Pt/Gr and Pt/BG, respectively.

3.3.1. Power Law Model

The power law model contained three unknown parameters (k, α, and β), as shown in Eq. (16) .

$$r_{NO} = kC_{NO}^{\alpha}C_{H_2}^{\beta} \quad (16)$$

where r_{NO} is the steady-state reaction rate of nitric oxide. C_{NO} and C_{H_2} are the steady-state concentrations of nitric oxide and hydrogen, respectively. k is the reaction rate constant. α and β are the apparent reaction orders with respect to nitric oxide and hydrogen, respectively. The fitting results by nonlinear least squares regression analysis with reaction data (Table 1) and rate expression (Eq. (16)) are listed in Table 3. Satisfied adjusted R^2 degrees were obtained for both Pt/Gr and Pt/BG at all four temperature points, indicating that the model was well fitted. Moreover, in all cases, the reaction rate exhibited a negative-order dependence on NO with the value of α -0.16~-0.19 while positive values were observed for H_2 (β located in the range of 0.77-1.40). The similar apparent reaction orders were also reported by other groups over Rh- (-0.22 for α, 0.59 for β) and Pd-based (-0.44 for α, 1.03 for β) catalysts [28, 32]. It highlighted the fact that both reactants demonstrated effect on the reaction rate, where NO restrained the reaction rate while H_2 enhanced the rate. In addition, the apparent activation energies (E_a) of the reaction over Pt/Gr and Pt/BG were determined to be 42.6±13.5 and 38.0±13.4 kJ mol^{-1}, respectively (Figure S13 and Figure S14 for details). The values are close to the one achieved over the $Pt/LaCoO_3$ (46.0 kJ mol^{-1}) [34], while lower than the ones obtained over the Rh/SiO_2 (13 kcal

mol^{-1}, i.e. -54.34 kJ mol^{-1}) [28] and Pd/Al_2O_3 (68.1 kJ mol^{-1}) or $Pd/LaCoO_3$ (79.7 kJ mol^{-1}) [32], which can be attributed to the superior activity of Pt catalysts for NO-H_2 reaction [2, 3].

Table 3 Results of nonlinear least squares regression based on power law expressions

T	Pt/Gr				Pt/BG			
(K)	$k \times 10^{-3}$	α	β	Adj. R^2	$k \times 10^{-3}$	α	β	Adj. R^2
300	1.39±0.23	-0.19±0.012	0.94±0.083	0.91	1.00±0.15	-0.18±0.010	0.77±0.063	0.95
310	3.47±0.57	-0.17±0.011	1.21±0.118	0.95	2.35±0.35	-0.17±0.009	1.04±0.090	0.93
320	4.91±0.64	-0.16±0.011	1.30±0.123	0.92	3.11±0.53	-0.16±0.011	1.11±0.105	0.96
330	7.03±0.99	-0.17±0.013	1.40±0.102	0.97	4.30±0.56	-0.18±0.012	1.22±0.111	0.92

3.3.2. L-H Kinetic Model

The Eley-Rideal mechanism was excluded due to the failure on the fitting of experimental data with the derived rate expression as listed in Supporting Information. The firm bonding of both NO and H_2 over the Pt/Gr and Pt/BG indicated Langmuir-Hinshelwood mechanism can be utilized to explain experimental observations and further develop extensive kinetic models for NO-H_2 reaction over two catalysts. As discussed in the *Introduction* section, the controversial N-O bond activation step, usually considered as the rate-determining step, would result in different kinetic rate expressions. Therefore, five models were developed in this work or adopted from the literature as listed in Table 4. The scenario with O vacancy involved (i.e. Eq. (7)) was excluded since it's not related to the current catalytic system. Other elementary steps contributing to the kinetic expressions developed in the five models include H_2 dissociative adsorption (Eq. (17)) on Pt site (denoted as *), NO adsorption (Eq. (18)) on Pt site, and H_2 molecular adsorption (Eq. (19))

on Pt site. All these steps are assumed to occur at equilibrium. The detailed derivation procedures for each expression are provided in Supporting Information.

$$H_2 + 2* \leftrightarrow 2\mathrm{H}* \quad (17)$$

$$\mathrm{NO} + * \leftrightarrow \mathrm{NO}* \quad (18)$$

$$H_2 + * \leftrightarrow H_2* \quad (19)$$

Table 4 Kinetic rate expressions based on different NO activation steps

Eq.	Activation Step	Expression	Ref.
(1)	$\mathrm{NO}* + * \rightarrow \mathrm{N}* + \mathrm{O}*$	$r_{NO} = \frac{k_1 K_{18}[NO]}{\left(1+\sqrt{K_{17}[H_2]}+K_{18}[NO]\right)^2}$	This work
(2)	$\mathrm{NO}* + \mathrm{NO}* \rightarrow N_2\mathrm{O}* + \mathrm{O}* + *$	$r_{NO} = \frac{k_2 K_{18}^2[NO]^2}{\left(1+\sqrt{K_{17}[H_2]}+K_{18}[NO]\right)^2}$	This work
(3)	$\mathrm{NO}* + \mathrm{H}* \rightarrow \mathrm{N}* + \mathrm{OH}*$	$r_{NO} = \frac{k_3\sqrt{K_{17}[H_2]}K_{18}[NO]}{\left(1+\sqrt{K_{17}[H_2]}+K_{18}[NO]\right)^2}$	This work
(5)	$\mathrm{HNO}* + \mathrm{H}* \rightarrow * \mathrm{HNOH}*$	$r_{NO} = \frac{k_5 K_4 K_{17}[H_2]K_{18}[NO]}{\left(1+\sqrt{K_{17}[H_2]}+K_{18}[NO]\right)^2}$	[35]
(6)	$\mathrm{NO}* + H_2* \rightarrow \mathrm{NH}* + \mathrm{OH}*$	$r_{NO} = \frac{2k_6 K_{19}[H_2]K_{NO}[NO]}{(1+K_{19}[H_2]+K_{18}[NO])^2}$	[32]

Three facts rule out the expression based on Eq. (1) for NO-H_2 reaction over the Pt/Gr or Pt/BG. No other species, especially N_2 or O_2, than NO was detected in the effluent stream during NO-TPD, indicating the chance for the reaction (1) is very low. DFT calculations indicated that no nitric oxide dissociative adsorption was observed, further denied the reaction. Moreover, the expression disagrees with a positive reaction order obtained for H_2 in power law model. Eq. (2)

was also excluded due to the similar reasons for the case (1), while the expression would derivate positive reaction order for NO which is not true in the power law model. Eq. (5) was no longer considered for further mathematical coverages due to the fact that no NH_3 was detected in the outlet during the reaction test, while NH_3 may be one of the byproducts based on this mechanism [35]. Based on current DFT calculations and reported experimental investigations [24, 25, 36], H_2 dissociative adsorption is much more dominant than molecular one over Pt sites. As a result, Eq. (6) was cancelled for further evaluation. Therefore, the rate expression derived from Eq. (3) was selected to fit the kinetic data in Table 1 by using the procedure mentioned in *2.3. Kinetics Data Analysis*. The Pt/Gr case showed a reasonable agreement between predicted reaction rate and the experimental one as shown in the parity plots (Figure 2).

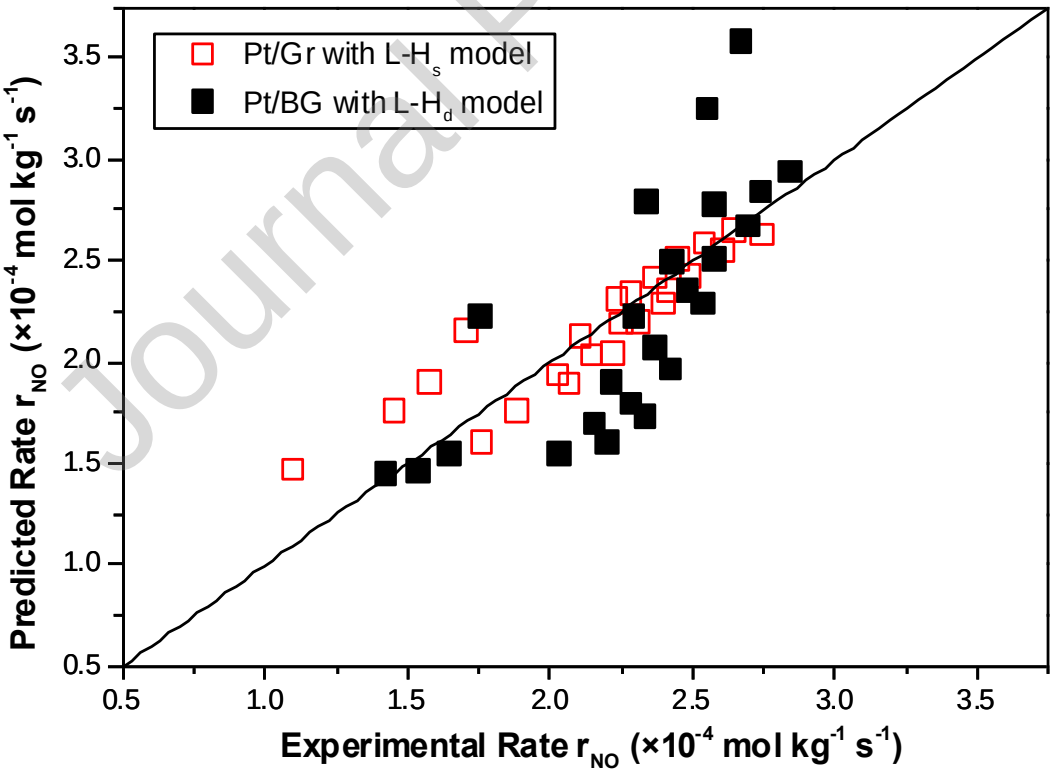

Figure 2. Parity plot of the experimental and the predicted reaction rates.

Unexpectedly, the expression did not fit the experimental data over the Pt/BG. Obviously, only Pt clusters were recognized as the active sites for NO/H_2 adsorption during above rate expression derivation procedure, which is a typical Langmuir-Hinshelwood single-site mechanism and true for the Pt/Gr case. However, both NO-TPD and DFT calculations indicated that two types of sites are available for NO chemisorption, which may lead to a Langmuir-Hinshelwood dual-site mechanism. Moreover, H-spillover has to be included for the rate expression development. Therefore, two additional elementary steps were reasonably proposed: NO adsorption on doped-boron site (denoted as #) at equilibrium (Eq. (20)) and NO# activation by H-spillover migrating from H-adsorbed on Pt site (Eq. (21)).

$$\mathrm{NO} + \# \leftrightarrow \mathrm{NO}\# \tag{20}$$

$$\mathrm{NO}\# + \mathrm{H}* \rightarrow \mathrm{N}\# + \mathrm{OH}* \tag{21}$$

As a result, the rate expression with respect to NO of NO-H_2 reaction over the Pt/BG can be described by the following equation (see Supporting Information for the derivation details), where γ is the ratio of H-spillover obtained from H_2-TPD, i.e. 0.1887.

$$r_{NO} = r_3 + r_{21} = \frac{(1-\gamma)k_3\sqrt{K_{17}[H_2]}K_{18}[NO]}{\left(1+\sqrt{K_{17}[H_2]}+K_{18}[NO]\right)^2} + \frac{\gamma k_{21}\sqrt{K_{17}[H_2]}K_{20}[NO]}{\left(1+\sqrt{K_{17}[H_2]}+K_{18}[NO]\right)(1+K_{20}[NO])}$$

$$= \left(\frac{(1-\gamma)k_3\sqrt{K_{17}[H_2]}K_{18}[NO](1+K_{20}[NO]) + \gamma k_{21}\sqrt{K_{17}[H_2]}K_{20}[NO]\left(1+\sqrt{K_{17}[H_2]}+K_{18}[NO]\right)}{\left(1+\sqrt{K_{17}[H_2]}+K_{18}[NO]\right)^2(1+K_{20}[NO])}\right)$$

The expression fits well with the reaction data of the Pt/BG as illustrated in Figure 2. Therefore, mathematical coverages are successfully achieved for NO-H_2 reaction over the Pt/Gr and Pt/BG with L-H_s and L-H_d model, respectively. Both models were further evaluated from the physical point of view. The estimated kinetic parameters for both models are listed in Table 5.

Pre-exponential factors A, activation energy E_a, and adsorption enthalpy ΔH and entropy ΔS of NO and H_2 were further derived by linear regression (Figure S15-S22) as described in section *2.3. Kinetics Data Analysis*. For the Pt/Gr, the determined ΔH and ΔS met the criteria as shown in Eq. (14) and (15). Moreover, the values of ΔH (-65.3±19.6 and -98.0±11.6 kJ mol^{-1} for H_2 and NO, respectively) are in good agreement to those (-59 and -77 kJ mol^{-1} for H_2 and NO, respectively) reported by Frank et al., where the authors investigated the kinetics and mechanism of NO-H_2 reaction under lean-burn conditions over a Pt-Mo-Co/α-Al_2O_3 catalyst [29]. The enthalpies are close to the adsorption energies calculated in the above DFT calculations (-60.7 and -198.1 kJ mol^{-1} for H_2 and NO, respectively) as listed in Table 2, while having the same tendency. Both kinetic modelling and DFT calculations showed that higher adsorption enthalpies/energies were observed over NO than those of H_2, which may account for its negative reaction order in the kinetics. In the current DFT calculations, the NO/H_2 co-adsorption configuration consists of only one NO and one H_2 molecular over Pt_{13} clusters, which is an ideal condition, while much more complicated conditions exist in the experiments. As a result, different values were obtained from theoretical and experimental investigations. The activation energy for N-O bond cleavage is 31.9±7.2 kJ mol^{-1}, which is much lower than those in the literature (63 and 93 kJ mol^{-1}) [29, 90]. It can be attributed to the different activation modes proposed between the current work and the reported ones. H-assisted NO* activation (Eq. (3)) was selected here while direct NO* dissociation (Eq. (1)) was adopted before.

For the Pt/BG case, obtained ΔH and ΔS values also met the constraints as illustrated by Eq. (14) and (15). The enthalpy values for NO/H_2 adsorption over Pt clusters (-82.8±43.5 and -51.0±8.4 kJ mol^{-1} for NO and H_2, respectively) are also close to the reported work [29]. Moreover, the adsorption enthalpy of NO over doped-boron was determined to be -86.5±12.8 kJ

mol^{-1}. It is lower than that over the Pt/Gr (-98.0±11.6 kJ mol^{-1}) while higher than that attached on Pt sites in the Pt/BG. Again, much lower values were measured from the experimental than DFT calculations (Pt_4, -191.1, BG, -230.9, and Pt_{13} -198.1 kJ mol^{-1}, respectively), which may be attributed to the different conditions experienced for two scenarios as discussed above. The activation energy of H-assisted NO* activation reaction over Pt clusters (19.9±3.9 kJ mol^{-1}) is much lower than that on doped-boron site (60.7±21.6 kJ mol^{-1}). It may be attributed to different types of active H provided in two reactions. For Pt clusters, NO was attacked by adjacent native H while in the latter case NO was activated by foreign H-spillover migrated from Pt clusters which made it more difficult. However, the reaction constant over the doped-boron site is still high due to its much larger pre-exponential factor (1.61×10^{12}±131 mol kg^{-1} s^{-1}) than that over Pt clusters (232.8±4.2 mol kg^{-1} s^{-1}), which leads to a considerable contribution of doped-boron for NO activation when compared to that from Pt clusters as shown in Table S3 and Figure 3. The reaction rate attributed to doped-boron site accounts for up to 51.5% of the overall rate equation. The kinetic modelling further confirmed the hypothesis made in the experimental observations and DFT calculations that two different mechanisms, i.e. Langmuir-Hinshelwood single-site and dual-site, are responsible for the Pt/Gr and Pt/BG, respectively. For the Pt/Gr, NO/H_2 co-adsorbs on Pt cluster while N-O bond activation follows H-assisted NO* route. For the Pt/BG, nitric oxide chemisorbs on both Pt and doped-boron sites, while they are activated by native H-adsorption and foreign H-spillover, respectively. The different elementary steps of $NO-H_2$ reaction over Pt/BG and Pt/Gr were summarized in Table S4, respectively, illustrating the different reaction mechanisms over the two catalysts.

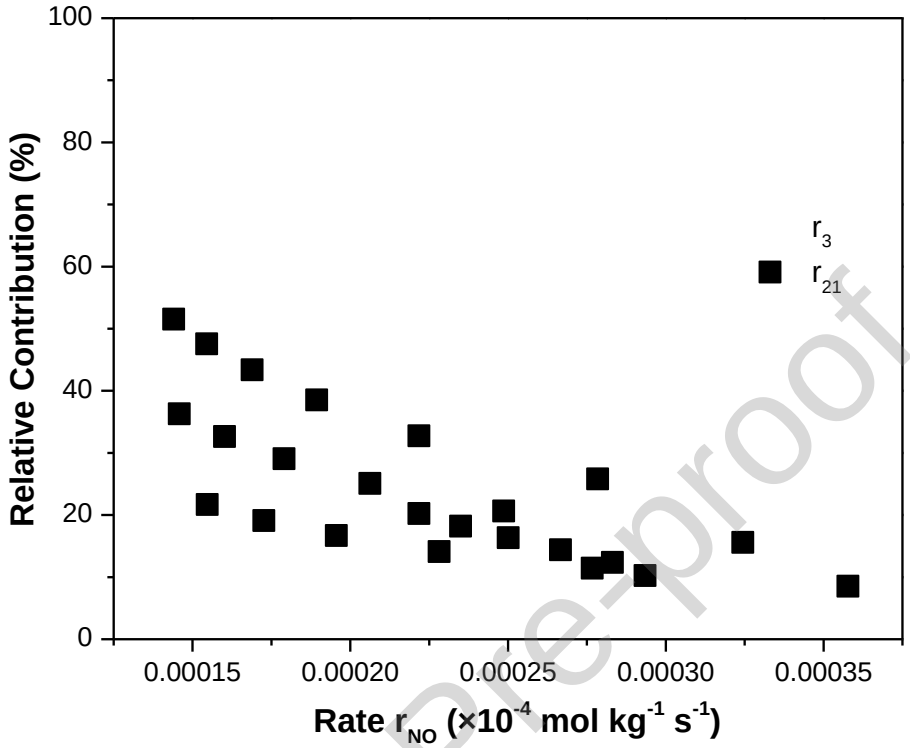

Figure 3. Contribution of Pt clusters (▫ r_3) and doped-boron (▮ r_{21}) for NO activation in NO-H_2 reaction over Pt/BG catalyst.

4. Conclusion

In this work, we present a combined experimental and theoretical study to reveal the mechanism of NO-H_2 reaction over the Pt/boron-doped graphene (Pt/BG) catalyst. Compared to the pristine graphene support, boron doping in graphene contributed to creating defect sites, decreasing Pt clusters size, facilitating hydrogen spillover, and providing additional sites for NO adsorption. Therefore, two models with 4 and 13 Pt atoms as clusters supported on boron-doped graphene and graphene sheet were rationally proposed for Pt/BG and Pt/Gr, respectively. DFT calculations further indicated that two different types of adsorption modes were observed on the

Pt/Gr and Pt/BG. NO/H_2 co-adsorbed over Pt_{13} clusters in the Pt/Gr. NO chemisorbed on both Pt_4 and doped-boron sites while H_2 dissociatively adsorbed over Pt_4 clusters with spillover in the Pt/BG. Moreover, Langmuir-Hinshelwood single-site and dual-site based kinetic models were successfully developed for NO-H_2 reaction over the Pt/Gr and Pt/BG catalysts, respectively. The kinetic findings further confirmed the experimental observations and the DFT calcualtions. This work provides new insights into NO-H_2 reaction over Pt/BG and Pt/Gr catalysts in a closely mechanistic view. The future work may focus on a complex catalytic system simulation, which aims to fully understand the important reaction for environment protection purpose.

Acknowledgements

Startup package financial support from Jianghan University is greatly appreciated. This work is supported by the Major Project of Hubei Province Technology Innovation Program (2019ACA160) and National Natural Science Foundation of China (NSFC) (grant number, 21506108).

Table 5 Estimated kinetic parameters with their 95% confidence intervals for both models

Sample	Constant	Temperature (K) 300	310	320	330	A (mol kg^{-1} s^{-1})	E_a (kJ mol^{-1})	ΔH (kJ mol^{-1})	ΔS (J mol^{-1} K^{-1})
Pt/Gr	K_{17}	30.1±3.2	8.15±1.29	6.88±0.84	2.42±0.31			-65.3±19.6	-106.7±62.4
	K_{18}	101.2±12.1	57.5±6.9	24.15±2.3	9.77±1.08			-98.0±11	-176.4±36.

							.6	6
	$k_3\times10^{-3}$	1.53±0.23	2.88±0.34	3.63±0.46	5.38±0.44	617.5±7.9	31.9±7.2	
Pt/BG	$K_{17}\times10^{-2}$	20.2±1.1	10.3±0.51	6.5±0.35	2.84±0.19		-51.0±8.4	-116.5±27.0
	K_{18}	1631±197	1112±135	419±51	61.7±9.5		-82.8±43.5	-145.1±139.1
	$K_{20}\times10^{-3}$	108±5.6	44.5±3.8	14.1±0.96	3.79±0.44		-86.5±12.8	-165.0±41.5
	$k_3\times10^{-1}$	0.80±0.03	1.03±0.05	1.38±0.04	1.56±0.08	232.8±4.2	19.9±3.9	
	k_{21}	53.6±4.1	88.9±3.7	179±6.1	569±46.1	1.61×10^{12}±131	60.7±21.6	

Reference

[1] Z. Liu, M. Wang, S. Liu, Z. Chen, L. Yang, K. Sun, Y. Chen, L. Zeng, W. Wang, J. Zhao, G. Sun, B. Liu, Y. Pan, Y. Liu, C. Liu, Design of assembled composite of Mn_3O_4@Graphitic carbon porous nano-dandelions: A catalyst for Low–temperature selective catalytic reduction of NOx with remarkable SO_2 resistance, Appl. Catal., B, 269 (2020) 118731.

[2] M. Piumetti, S. Bensaid, D. Fino, N. Russo, Catalysis in Diesel engine NOx aftertreatment: a review, Catal., Struct. React., 1 (2015) 155-173.

[3] Z. Hu, R.T. Yang, 110th Anniversary: Recent Progress and Future Challenges in Selective Catalytic Reduction of NO by H_2 in the Presence of O_2, Ind. Eng. Chem. Res., 58 (2019) 10140-10153.

[4] W. Si, H. Liu, T. Yan, H. Wang, C. Fan, S. Xiong, Z. Zhao, Y. Peng, J. Chen, J. Li, Sn-doped rutile TiO_2 for vanadyl catalysts: Improvements on activity and stability in SCR reaction, Appl. Catal., B, 269 (2020) 118797.

[5] R. Daya, S.Y. Joshi, J. Luo, R.K. Dadi, N.W. Currier, A. Yezerets, On kinetic modeling of change in active sites upon hydrothermal aging of Cu-SSZ-13, Appl. Catal., B, 263 (2020) 118368.

[6] J. Luo, K. Kamasamudram, N. Currier, A. Yezerets, NH_3-TPD methodology for quantifying hydrothermal aging of Cu/SSZ-13 SCR catalysts, Chem. Eng. Sci., 190 (2018) 60-67.

[7] G. Xu, J. Ma, L. Wang, W. Xie, J. Liu, Y. Yu, H. He, Insight into the origin of sulfur tolerance of Ag/Al_2O_3 in the H_2-C_3H_6-SCR of NOx, Appl. Catal., B, 244 (2019) 909-918.

[8] N. Shi, B.-s. Tu, W. Sun, J.-y. Liu, L.-m. Cao, X.-q. Gong, J. Yang, Room temperature efficient reduction of NOx by H_2 in a permeable compounded membrane – Catalytic reactor, Chem. Eng. J., 283 (2016) 929-935.

[9] H. Yuan, N. Sun, J. Chen, J. Jin, H. Wang, P. Hu, Insight into the NH_3-Assisted Selective Catalytic Reduction of NO on β-MnO2(110): Reaction Mechanism, Activity Descriptor, and Evolution from a Pristine State to a Steady State, ACS Catal., 8 (2018) 9269-9279.

[10] W.-C. Ding, X.-K. Gu, H.-Y. Su, W.-X. Li, Single Pd Atom Embedded in CeO_2(111) for NO Reduction with CO: A First-Principles Study, J. Phys. Chem. C, 118 (2014) 12216-12223.

[11] Y. Yang, J. Liu, F. Liu, Z. Wang, J. Ding, H. Huang, Reaction mechanism for NH_3-SCR of NOx over $CuMn_2O_4$ catalyst, Chem. Eng. J., 361 (2019) 578-587.

[12] L. Wang, H. Chen, M.-H. Yuan, S. Rivillon, E.H. Klingenberg, J.X. Li, R.T. Yang, Selective catalytic reduction of nitric oxide by hydrogen over Zn-ZSM-5 and Pd and Pd/Ru based catalysts, Appl. Catal., B, 152-153 (2014) 162-171.

[13] Z. Liu, Y. Lu, L. Yuan, L. Ma, L. Zheng, J. Zhang, T. Hu, Selective catalytic reduction of NOx with H_2 over WO_3 promoted Pt/TiO_2 catalyst, Appl. Catal., B, 188 (2016) 189-197.

[14] C.N. Costa, P.G. Savva, C. Andronikou, P.S. Lambrou, K. Polychronopoulou, V.C. Belessi, V.N. Stathopoulos, P.J. Pomonis, A.M. Efstathiou, An Investigation of the $NO/H_2/O_2$ (Lean De-NOx) Reaction on a Highly Active and Selective $Pt/La_{0.7}Sr_{0.2}Ce_{0.1}FeO_3$ Catalyst at Low Temperatures, J. Catal., 209 (2002) 456-471.

[15] P.G. Savva, C.N. Costa, Hydrogen Lean-DeNOx as an Alternative to the Ammonia and Hydrocarbon Selective Catalytic Reduction (SCR), Cat. Rev., 53 (2011) 91-151.

[16] W. Sun, K. Qiao, J.-y. Liu, L.-m. Cao, X.-q. Gong, J. Yang, Pt-Doped $NiFe_2O_4$ Spinel as a Highly Efficient Catalyst for H_2 Selective Catalytic Reduction of NO at Room Temperature, ACS. Comb. Sci., 18 (2016) 195-202.

[17] Z. Hu, X. Yong, D. Li, R.T. Yang, Synergism between palladium and nickel on $Pd\text{-}Ni/TiO_2$ for H_2-SCR: A transient DRIFTS study, J. Catal., 381 (2020) 204-214.

[18] X. Wang, X. Wang, H. Yu, X. Wang, The functions of Pt located at different positions of HZSM-5 in H_2-SCR, Chem. Eng. J., 355 (2019) 470-477.

[19] Y. Xue, W. Sun, Q. Wang, L. Cao, J. Yang, Sparsely loaded Pt/MIL-96(Al) MOFs catalyst with enhanced activity for H_2-SCR in a gas diffusion reactor under 80 °C, Chem. Eng. J., 335 (2018) 612-620.

[20] K. Duan, Z. Wang, C. Hardacre, Z. Liu, S. Chansai, C. Stere, Promoting effect of Au on Pd/TiO_2 catalyst for the selective catalytic reduction of NOx by H_2, Catal. Today, 332 (2019) 69-75.

[21] C.-G. Liu, Y.-J. Chu, L.-L. Zhang, C. Sun, J.-Y. Shi, Reduction of N_2O by H_2 Catalyzed by Keggin–Type Phosphotungstic Acid Supported Single-Atom Catalysts: An Insight from Density Functional Theory Calculations, Environ. Sci. Technol., 53 (2019) 12893-12903.

[22] C. Xu, W. Sun, L. Cao, T. Li, X. Cai, J. Yang, Highly efficient Pd-doped aluminate spinel catalysts with different divalent cations for the selective catalytic reduction of NO with H_2 at low temperature, Chem. Eng. J., 308 (2017) 980-987.

[23] Z. Hong, Z. Wang, D. Chen, Q. Sun, X. Li, Hollow ZSM-5 encapsulated Pt nanoparticles for selective catalytic reduction of NO by hydrogen, Appl. Surf. Sci., 440 (2018) 1037-1046.

[24] C.N. Costa, A.M. Efstathiou, Low-temperature H_2-SCR of NO on a novel $Pt/MgO-CeO_2$ catalyst, Appl. Catal., B, 72 (2007) 240-252.

[25] C.N. Costa, A.M. Efstathiou, Mechanistic Aspects of the H_2-SCR of NO on a Novel $Pt/MgO{-}CeO_2$ Catalyst, J. Phys. Chem. C, 111 (2007) 3010-3020.

[26] L. Wang, C. Yin, R.T. Yang, Selective catalytic reduction of nitric oxide with hydrogen on supported Pd: Enhancement by hydrogen spillover, Appl. Catal., A, 514 (2016) 35-42.

[27] Rajbala, D. Bhatia, Crystallite-scale model for NOx reduction by hydrogen spillover on SBA-15 and MCM-41, Catal. Today, (2020).

[28] W.C. Hecker, A.T. Bell, Reduction of NO by H_2 over silica-supported rhodium: Infrared and kinetic studies, J. Catal., 92 (1985) 247-259.

[29] B. Frank, G. Emig, A. Renken, Kinetics and mechanism of the reduction of nitric oxides by H2 under lean-burn conditions on a Pt–Mo–Co/α-Al_2O_3 catalyst, Appl. Catal., B, 19 (1998) 45-57.

[30] R. Burch, A.A. Shestov, J.A. Sullivan, A Transient Kinetic Study of the Mechanism of the NO+H_2 Reaction over Pt/SiO_2 Catalysts: 1. Isotopic Transient Kinetics and Temperature Programmed Analysis, J. Catal., 186 (1999) 353-361.

[31] F. Dhainaut, S. Pietrzyk, P. Granger, Kinetic investigation of the NO reduction by H_2 over noble metal based catalysts, Catal. Today, 119 (2007) 94-99.

[32] F. Dhainaut, S. Pietrzyk, P. Granger, Kinetics of the NO+H_2 reaction over supported noble metal based catalysts: Support effect on their adsorption properties, Appl. Catal., B, 70 (2007) 100-110.

[33] F. Dhainaut, S. Pietrzyk, P. Granger, NO + H_2 reaction on Pd/Al_2O_3 under lean conditions: kinetic study, Top. Catal., 42 (2007) 135-141.

[34] F. Dhainaut, S. Pietrzyk, P. Granger, Kinetics of the NO/H_2 reaction on Pt/$LaCoO_3$: A combined theoretical and experimental study, J. Catal., 258 (2008) 296-305.

[35] D.D. Hibbitts, R. Jiménez, M. Yoshimura, B. Weiss, E. Iglesia, Catalytic NO activation and NO–H_2 reaction pathways, J. Catal., 319 (2014) 95-109.

[36] C. Hahn, M. Endisch, F.J.P. Schott, S. Kureti, Kinetic modelling of the NOx reduction by H_2 on Pt/WO_3/ZrO_2 catalyst in excess of O_2, Appl. Catal., B, 168-169 (2015) 429-440.

[37] C. Hahn, M. Endisch, S. Kureti, Elementary Kinetic Mean Field Modelling of the Lean NOx Reduction by H_2 on Pt/WO_3/ZrO_2 Catalyst, Top. Catal., 60 (2017) 238-242.

[38] C.A. Farberow, J.A. Dumesic, M. Mavrikakis, Density Functional Theory Calculations and Analysis of Reaction Pathways for Reduction of Nitric Oxide by Hydrogen on Pt(111), ACS Catal., 4 (2014) 3307-3319.

[39] L.-y. Huai, T. Su, H. Wen, X. Jin, J.-y. Liu, NO Reduction by H_2 on the Rh(111) and Rh(221) Surfaces: A Mechanistic and Kinetic Study, J. Phys. Chem. C, 120 (2016) 5410-5419.

[40] L. Ling, Z. Zhao, X. Feng, Q. Wang, B. Wang, R. Zhang, D. Li, Insight into the Reduction of NO by H_2 on the Stepped Pd(211) Surface, J. Phys. Chem. C, 121 (2017) 16399-16414.

[41] Y. Bai, M. Mavrikakis, Mechanistic Study of Nitric Oxide Reduction by Hydrogen on Pt(100) (I): A DFT Analysis of the Reaction Network, J. Phys. Chem. B, 122 (2018) 432-443.

[42] H. Wen, L.-y. Huai, X. Jin, J.-y. Liu, Mechanism of Nitric Oxide Reduction by Hydrogen on Ni(110) and Ir/Ni(110): First Principles and Microkinetic Modeling, J. Phys. Chem. C, 123 (2019) 4825-4836.

[43] K. Tomishige, K. Asakura, Y. Iwasawa, Observation of Molecular Reaction Intermediate and Reaction Mechanism for NO Dissociation and NO-H_2 Reaction on Rh-Sn/SiO_2 Catalysts, J. Catal., 157 (1995) 472-481.

[44] A. Kumar, V. Medhekar, M.P. Harold, V. Balakotaiah, NO decomposition and reduction on Pt/Al_2O_3 powder and monolith catalysts using the TAP reactor, Appl. Catal., B, 90 (2009) 642-651.

[45] B.E. Nieuwenhuys, The Surface Science Approach Toward Understanding Automotive Exhaust Conversion Catalysis at the Atomic Level, in: W.O. Haag, B.C. Gates, H. Knözinger (Eds.) Adv. Catal., Academic Press, 1999, pp. 259-328.

[46] C.N. Costa, P.G. Savva, J.L.G. Fierro, A.M. Efstathiou, Industrial H_2-SCR of NO on a novel Pt/MgO–CeO_2 catalyst, Appl. Catal., B, 75 (2007) 147-156.

[47] Y. Zhang, H. Zeng, B. Jia, Z. Wang, Z. Liu, Selective catalytic reduction of NOx by H_2 over Pd/TiO_2 catalyst, Chin. J. Catal., 40 (2019) 849-855.

[48] M. Hu, Z. Yao, L. Li, Y.-H. Tsou, L. Kuang, X. Xu, W. Zhang, X. Wang, Boron-doped graphene nanosheet-supported Pt: a highly active and selective catalyst for low temperature H_2-SCR, Nanoscale, 10 (2018) 10203-10212.

[49] M. Hu, Z. Yao, X. Liu, L. Ma, Z. He, X. Wang, Enhancement mechanism of hydroxyapatite for photocatalytic degradation of gaseous formaldehyde over TiO_2/hydroxyapatite, J. Taiwan Inst. Chem. Eng,, 85 (2018) 91-97.

[50] J. Palau, J.M. Penya-Roja, C. Gabaldón, F. Javier Álvarez-Hornos, F. Sempere, V. Martínez-Soria, UV photocatalytic oxidation of paint solvent compounds in air using an annular TiO_2-supported reactor, J. Chem. Technol. Biotechnol., 86 (2011) 273-281.

[51] U. Oemar, A. Ming Li, K. Hidajat, S. Kawi, Mechanism and kinetic modeling for steam reforming of toluene on $La_{0.8}Sr_{0.2}Ni_{0.8}Fe_{0.2}O_3$ catalyst, AIChE J., 60 (2014) 4190-4198.

[52] H.S. Fogler, Elements of Chemical Reaction Engineering (Fourth Edition), Prentice-Hall, 2006.

[53] L. Zhang, W. Fu, Q. Yu, T. Tang, Y. Zhao, H. Zhao, Y. Li, Ni_2P clusters on zeolite nanosheet assemblies with high activity and good stability in the hydrodesulfurization of 4,6-dimethyldibenzothiophene, J. Catal., 338 (2016) 210-221.

[54] D. Yuan, X. Li, Q. Zhao, J. Zhao, M. Tadé, S. Liu, A novel CuTi-containing catalyst derived from hydrotalcite-like compounds for selective catalytic reduction of NO with C_3H_6 under lean-burn conditions, J. Catal., 309 (2014) 268-279.

[55] C.N. Costa, V.N. Stathopoulos, V.C. Belessi, A.M. Efstathiou, An investigation of the $NO/H_2/O_2$ (Lean-deNOx) reaction on a highly active and selective $Pt/La_{0.5}Ce_{0.5}MnO_3$ catalyst, J. Catal., 197 (2001) 350-364.

[56] M. Hu, X. Wang, Effect of N_3^- species on selective acetylene hydrogenation over Pd/SAC catalysts, Catal. Today, 263 (2016) 98-104.

[57] T. Noor, Y. Qi, D. Chen, Hydrogen dependence of the reaction mechanism and kinetics of water gas shift reaction on Ni catalyst: Experimental and DFT study, Appl. Catal., B, 264 (2020) 118430.

[58] M. Hu, Z. Yao, K.N. Hui, K.S. Hui, Novel mechanistic view of catalytic ozonation of gaseous toluene by dual-site kinetic modelling, Chem. Eng. J., 308 (2017) 710-718.

[59] C. Huang, Y.Y. Li, L.P. Liu, H. Wu, M.H. Zong, W.Y. Lou, Kinetics and mechanism analysis on microbial oil production by Trichosporon fermentans in rice straw hydrolysate, Ind. Eng. Chem. Res., 53 (2014) 19034-19043.

[60] K. Baig, B. Kvamme, T. Kuznetsova, J. Bauman, Impact of water film thickness on kinetic rate of mixed hydrate formation during injection of CO_2 into CH_4 hydrate, AIChE J., 61 (2015) 3944-3957.

[61] G.F. Froment, Single event kinetic modeling of complex catalytic processes, Cat. Rev. - Sci. Eng. , 47 (2005) 83-124.

[62] G.F. Froment, On fundamental kinetic equations for chemical reactions and processes, Curr. Opin. Chem. Eng., 5 (2014) 1-6.

[63] S. Mukherjee, M.A. Vannice, Solvent effects in liquid-phase reactions II. Kinetic modeling for citral hydrogenation, J. Catal., 243 (2006) 131-148.

[64] M.P. Heynderickx, J.W. Thybaut, H. Poelman, D. Poelman, G.B. Marin, Kinetic modeling of the total oxidation of propane over CuO-CeO_2/γ-Al_2O_3, Appl. Catal., B, 95 (2010) 26-38.

[65] G. Kresse, J. Furthmüller, Efficiency of ab-initio total energy calculations for metals and semiconductors using a plane-wave basis set, Comput.Mater. Sci., 6 (1996) 15-50.

[66] G. Kresse, J. Furthmüller, Efficient iterative schemes for ab initio total-energy calculations using a plane-wave basis set, Phys. Rev. B, 54 (1996) 11169-11186.

[67] P. Hohenberg, W. Kohn, Inhomogeneous Electron Gas, Phys. Rev., 136 (1964) B864-B871.

[68] W. Kohn, L.J. Sham, Self-Consistent Equations Including Exchange and Correlation Effects, Phys. Rev., 140 (1965) A1133-A1138.

[69] P.E. Blöchl, Projector augmented-wave method, Phys. Rev. B, 50 (1994) 17953-17979.

[70] J.P. Perdew, K. Burke, M. Ernzerhof, Generalized Gradient Approximation Made Simple, Phys. Rev. Lett., 77 (1996) 3865-3868.

[71] D.J. Chadi, Special points for Brillouin-zone integrations, Phys. Rev. B, 16 (1977) 1746-1747.

[72] X. Bo, M. Li, C. Han, L. Guo, The influence of boron dopant on the electrochemical properties of graphene as an electrode material and a support for Pt catalysts, Electrochim. Acta, 114 (2013) 582-589.

[73] S. Zhang, B. Li, X. Wang, G. Zhao, B. Hu, Z. Lu, T. Wen, J. Chen, X. Wang, Recent developments of two-dimensional graphene-based composites in visible-light photocatalysis for eliminating persistent organic pollutants from wastewater, Chem. Eng. J., 390 (2020) 124642.

[74] X. Chen, W.-D. Oh, T.-T. Lim, Graphene- and CNTs-based carbocatalysts in persulfates activation: Material design and catalytic mechanisms, Chem. Eng. J., 354 (2018) 941-976.

[75] N.R. Stuckert, L. Wang, R.T. Yang, Characteristics of Hydrogen Storage by Spillover on Pt-Doped Carbon and Catalyst-Bridged Metal Organic Framework, Langmuir, 26 (2010) 11963-11971.

[76] I. Fampiou, A. Ramasubramaniam, CO Adsorption on Defective Graphene-Supported Pt_{13} Nanoclusters, J. Phys. Chem. C, 117 (2013) 19927-19933.

[77] I. Fampiou, A. Ramasubramaniam, Binding of Pt Nanoclusters to Point Defects in Graphene: Adsorption, Morphology, and Electronic Structure, J. Phys. Chem. C, 116 (2012) 6543-6555.

[78] A. Kuang, M. Mo, M. Kuang, B. Wang, C. Tian, H. Yuan, G. Wang, H. Chen, The comparative study of XO_2 (X = C, N, S) gases adsorption and dissociation on pristine and defective graphene supported Pt_{13}, Mater. Chem. Phys., 247 (2020) 122712.

[79] Y. Okamoto, Density-functional calculations of icosahedral M_{13} (M=Pt and Au) clusters on graphene sheets and flakes, Chem. Phys. Lett., 420 (2006) 382-386.

[80] I.N. Chen, S.-Y. Wu, H.-T. Chen, Hydrogen storage in N- and B-doped graphene decorated by small platinum clusters: A computational study, Appl. Surf. Sci., 441 (2018) 607-612.

[81] Mandeep, L. Sharma, R. Kakkar, DFT study on the adsorption of p-nitrophenol over vacancy and Pt-doped graphene sheets, Comput. Theor. Chem., 1142 (2018) 88-96.

[82] M. Kunaseth, P. Poldorn, A. Junkeaw, J. Meeprasert, C. Rungnim, S. Namuangruk, N. Kungwan, C. Inntam, S. Jungsuttiwong, A DFT study of volatile organic compounds adsorption on transition metal deposited graphene, Appl. Surf. Sci., 396 (2017) 1712-1718.

[83] N. Jin, J. Han, H. Wang, X. Zhu, Q. Ge, A DFT study of oxygen reduction reaction mechanism over O-doped graphene-supported Pt_4, Pt_3Fe and Pt_3V alloy catalysts, Int. J. Hydrogen Energy, 40 (2015) 5126-5134.

[84] C. Mager-Maury, G. Bonnard, C. Chizallet, P. Sautet, P. Raybaud, H_2-Induced Reconstruction of Supported Pt Clusters: Metal–Support Interaction versus Surface Hydride, ChemCatChem, 3 (2011) 200-207.

[85] R. Faccio, L. Fernández-Werner, H. Pardo, C. Goyenola, O.N. Ventura, Á.W. Mombrú, Electronic and Structural Distortions in Graphene Induced by Carbon Vacancies and Boron Doping, J. Phys. Chem. C, 114 (2010) 18961-18971.

[86] D.W. Boukhvalov, I.S. Zhidkov, A.I. Kukharenko, A.I. Slesarev, A.F. Zatsepin, S.O. Cholakh, E.Z. Kurmaev, Stability of boron-doped graphene/copper interface: DFT, XPS and OSEE studies, Appl. Surf. Sci., 441 (2018) 978-983.

[87] S. Kawai, S. Saito, S. Osumi, S. Yamaguchi, A.S. Foster, P. Spijker, E. Meyer, Atomically controlled substitutional boron-doping of graphene nanoribbons, Nat. Commun., 6 (2015) 8098.

[88] Z. Yao, M. Hu, Z. Iqbal, X. Wang, N_8^- Polynitrogen Stabilized on Boron-Doped Graphene as Metal-Free Electrocatalysts for Oxygen Reduction Reaction, ACS Catal., 10 (2020) 160-167.

[89] H.-Y. Wu, X. Fan, J.-L. Kuo, W.-Q. Deng, DFT Study of Hydrogen Storage by Spillover on Graphene with Boron Substitution, J. Phys. Chem. C, 115 (2011) 9241-9249.

[90] A. Lindholm, N.W. Currier, A. Yezerets, L. Olsson, A kinetic study of NOx reduction over Pt/SiO_2 model catalysts with hydrogen as the reducing agent, Top. Catal., 42 (2007) 83-89.

Graphical abstract

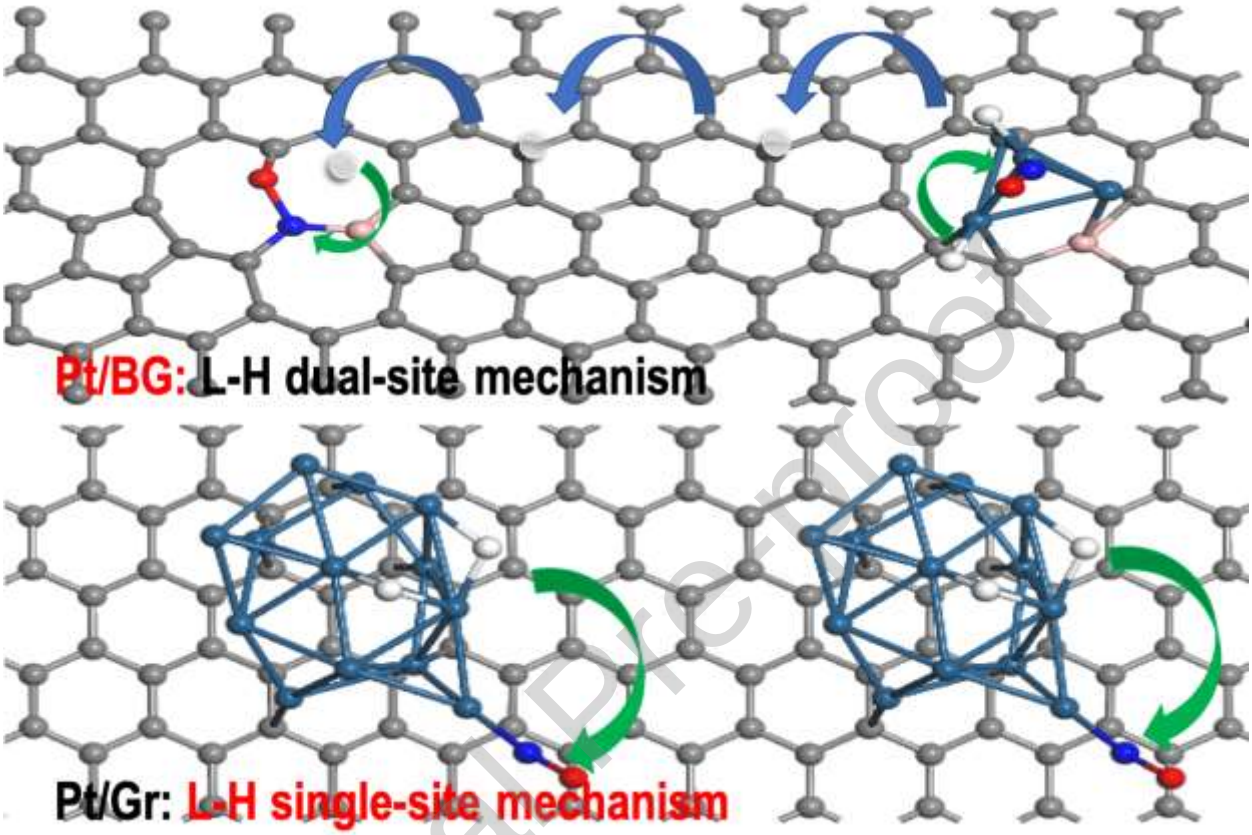

Credit Author Statement

Zhenhua Yao, Lei Li, Kwun Nam Hui, Maocong Hu: Conceptualization, Methodology, Software; **Zhenhua Yao, Xuguang Liu, Maocong Hu, K.S. Hui**: Writing- Original draft preparation. **Zhenhua Yao, Ling Shi, Furong Zhou**: Investigation; **Maocong Hu, Xuguang Liu, Ling Shi**: Funding acquisition; **Maocong Hu**: Supervision; **Maocong Hu, K.S. Hui**: Writing- Reviewing and Editing

Declaration of interests

☒ The authors declare that they have no known competing financial interests or personal relationships that could have appeared to influence the work reported in this paper.

☐The authors declare the following financial interests/personal relationships which may be considered as potential competing interests:

Highlights

- Systematic experimental and DFT study was conducted for NO-H_2 reaction
- Doped-boron of Pt/BG was identified as an additional adsorption site for NO
- Dual-site kinetic model was successfully developed for Pt/BG case
- Single-site kinetic model was adopted for Pt/Gr case
- H-assisted N-O cleavage was identified as the activation step